ACS Catalysis

RESEARCH ARTICLE

pubs.acs.org/acscatalysis

Synthesis of Highly Ordered Hydrothermally Stable Mesoporous Niobia Catalysts by Atomic Layer Deposition

Yomaira J. Pagán-Torres,[†] Jean Marcel R. Gallo,[†] Dong Wang,[†] Hien N. Pham,[‡] Joseph A. Libera,[§] Christopher L. Marshall,[⊥] Jeffrey W. Elam,[§] Abhaya K. Datye,[‡] and James A. Dumesic[†,*]

[†]Department of Chemical and Biological Engineering, University of Wisconsin−Madison, Madison, Wisconsin 53706, United States

[‡]Department of Chemical & Nuclear Engineering and Center for Microengineered Materials, University of New Mexico, Albuquerque, New Mexico 87131, United States

[§]Energy Systems Division, Argonne National Laboratory, Argonne, Illinois 60439, United States

[⊥]Chemical Sciences & Engineering Division, Argonne National Laboratory, Argonne, Illinois 60439, United States

S Supporting Information

ABSTRACT: A new class of mesoporous niobia catalysts has been synthesized by atomic layer deposition (ALD) of niobia within the pores of a mesoporous silica (SBA-15). Mesoporous materials after ALD cycles of niobia maintained the structural organization of SBA-15. Increasing loadings of niobia cause a decrease in the surface area, pore volume, and pore diameter due to the conformal coating of niobia within the pores. Materials containing 10, 19, and 30 cycles show remarkable hydrothermal stability, with minimal change in porosity and structural properties upon treatment in liquid water at 473 K. The mesoporous niobia material produced by 19 cycles has been studied as an acid catalyst for the gas-phase dehydration of 2-propanol, and for the dehydration of 2-butanol in both the gas and liquid phases, showing catalytic activity superior to commercial niobia (HY-340) per mass of material. Furthermore, deposition of Pd nanoparticles on this material consisting of SBA-15 coated with 19 cycles of niobia leads to a bifunctional catalyst for the transformation of γ-valerolactone to pentanoic acid, showing better stability versus time-on-stream compared to a conventional catalyst consisting of Pd supported on HY-340.

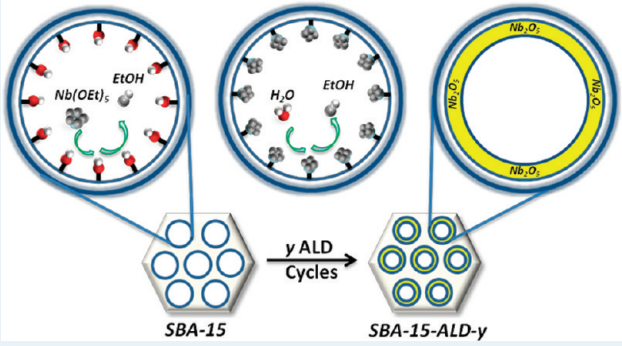

KEYWORDS: Catalysis, Mesoporous Materials, Surface Modification, Biomass

1. INTRODUCTION

Growing concerns regarding global climate change and diminishing fossil fuel resources have created interest in the transformation of biomass-derived carbohydrates to fuels and chemicals. An important challenge encountered in these processes is the synthesis of heterogeneous catalysts that can withstand liquid water at high temperatures (e.g., 473 K), conditions commonly encountered in the processing of biomass-derived oxygenated feedstocks (sugars and polyols).[1,2] Niobic acid ($Nb_2O_5 \cdot nH_2O$) catalysts have shown promise in important biomass reactions, such as dehydration, aldol condensation, hydrolysis, and ketonization, since few conventional solid acids possess the required acidity and stability to catalyze reactions in which water is used as the solvent or is involved as a reactant or a byproduct.[3−8] However, a limitation of niobia catalysts under hydrothermal conditions is its transformation from an amorphous to a crystalline phase (TT-phase), leading to a decrease in the surface area and catalytic activity.[9−11] In addition, it has been previously reported that phase transformation of niobia favors the sintering and encapsulation of supported nanoparticles.[12] Thus, the synthesis of hydrothermally stable and catalytically active niobia-based catalysts with high surface area is essential in the development of more efficient catalytic systems for aqueous-phase biomass processing.

High surface area transition metal oxides, including mesoporous niobium oxide, have been successfully synthesized by template-assisted self-assembly routes.[13−18] Despite their large pore volumes and high surface areas, these mesorporous niobium oxides lack catalytic activity due to decreased Brønsted and Lewis acidity caused by calcination treatments for template removal.[19] Although efforts have been made to introduce acidity to these materials by treatment with sulfuric acid or phosphoric acid, the resultant materials suffer from severe deactivation due to leaching of acidic components and collapse of structural integrity.[19] Recently, Nakajima, et al. reported the synthesis of mesoporous niobia possessing both Brønsted and Lewis acid sites.[20] The templates

Received: July 11, 2011
Revised: August 9, 2011

 © XXXX American Chemical Society

were removed by solvent extraction rather than calcination. However, the resultant materials were studied for catalytic activity and stability only under mild conditions (373 K and ambient pressure).

Alternatively, high surface area transition metal oxides can be obtained by surface modification of mesoporous silica, such as SBA-15 and MCM-41, by liquid-phase grafting of metallic precursors.[21−26] However, it is difficult through these methods to control the composition and structure of the dispersed metal oxide species.[27] Molecularly dispersed species are obtained with a single grafting step at low loadings, whereas multiple grafting and postsynthesis treatment steps are required if polymeric species are desired.[28] To the best of our knowledge, the complete surface coating of mesoporous silica with niobia has not yet been reported.

In this work, we report a facile one-pot coating method for the synthesis of mesoporous niobia employing atomic layer deposition (ALD) of niobia within the pores of a mesoporous silica scaffold, SBA-15. The application of atomic layer deposition with selected precursors offers atomic-level control over the composition and structure of the surface niobium oxide species created. The self-limiting nature of the gas-phase reactions occurring during ALD allows for the uniform coating of all exposed surfaces of SBA-15 with monolayer thickness control.[29,30] Compared with liquid-phase grafting, high niobia loadings can be achieved simply by increasing the number of ALD cycles, which is done in a continuous manner with no postsynthesis treatment steps needed. The composition and structural properties of the synthesized mesoporous niobia materials were characterized in the present paper by X-ray diffraction (XRD), scanning transmission electron microscopy (STEM), N_2 physisorption, FTIR, Raman spectroscopy, and NH_3 temperature programmed desorption (TPD). The resultant materials combine the highly ordered porous structure of SBA-15 with the surface properties of niobia and demonstrate remarkable hydrothermal stability in liquid water at elevated temperature (e.g., 473 K) and pressure.

We have studied the catalytic properties of these niobia-based materials for the gas-phase dehydration of 2-propanol, a standard probe reaction used to assess the acidic properties of heterogeneous catalysts. Furthermore, to explore their potential as solid acid catalysts suitable for aqueous-phase biomass processing, the reactivities and stabilities of the catalysts were studied for the acid-catalyzed dehydration of 2-butanol under processing conditions typical of aqueous-phase dehydration hydrogenation (APDH), used for deoxygenation of carbohydrates and sugar alcohols at high temperatures and pressures (e.g., 513 K and 50 bar). In addition, palladium particles were supported on these materials for the synthesis of a bifunctional catalyst for the conversion of γ-valerolactone (GVL) to pentanoic acid, requiring acidic sites for the ring-opening of GVL and metal particles for the hydrogenation of the reaction intermediate pentenoic acid to pentanoic acid. These platform chemicals can be further upgraded to fuel components by means of ketonization and decarboxylation/oligomerization reactions.[12,31]

2. EXPERIMENTAL SECTION

2.1. SBA-15 Synthesis. Mesoporous silica, SBA-15, was synthesized following the procedure of Zhao, et al.[32] In a typical synthesis, 4.0 g of Pluronic P123 (Aldrich) was dissolved in 120 g of 2 M HCl solution and 30 g of deionized H_2O while stirring at 308 K. Once dissolved, 8.50 g of tetraethoxysilane (TEOS, Aldrich) was added to the solution, followed by stirring for 20 h at 308 K. The resulting mixture was maintained at 373 K under static conditions for 24 h. The solid product was filtered, washed, and air-dried at room temperature. Template removal (P123) was accomplished by calcination in air at 773 K (ramp 1 K min^{-1}) for 6 h.

2.2. Atomic Layer Deposition of Niobia. Niobia was deposited by ALD in a viscous flow reactor at a temperature of 473 K.[33] Synthesized SBA-15 was placed in a shallow tray in a layer ~1 mm deep and covered with a tight fitting wire cloth lid to contain the SBA-15 while allowing access to the ALD precursor vapors.[34] The loaded tray was first heated in air at 473 K for 30 min to remove physisorbed moisture, weighed, and then inserted into the viscous flow ALD reactor. Ultrahigh purity (99.999%) nitrogen carrier gas was continuously passed through the reactor at a mass flow rate of 190 cm^3 (STP) min^{-1} and a pressure of 1.1 Torr. The ALD of Nb_2O_5 was performed using alternating exposures to niobium(V) ethoxide ($Nb(OCH_2CH_3)_5$) (Aldrich) and deionized H_2O. The $Nb(OCH_2CH_3)_5$ was held in a stainless steel bubbler heated to 408 K through which 100 cm^3 (STP) min^{-1} of nitrogen carrier gas was diverted for a period of 8 min. The H_2O was held in a stainless steel reservoir at room temperature, and the H_2O vapor was injected onto the flowing nitrogen at a rate of 25 cm^3 (STP) min^{-1} for a period of 4 min. Purge periods of 2 min were used between exposures to the ALD reactants. The trays were immediately weighed upon removal from the reactor and then allowed to cool in the laboratory air environment. Samples are denoted as SBA-15-ALD-*y*, where *y* corresponds to the number of niobia cycles performed (1, 10, 19, and 30). Commercial bulk amorphous niobia, HY-340, was obtained from CBMM Brazil.

2.3. Palladium-Supported Niobia Catalysts. Catalysts consisting of Pd (1 wt %) supported on SBA-15-ALD-19 and on commercial niobia, HY-340, were prepared by incipient wetness impregnation of an aqueous solution of $Pd(NO_3)_2 \cdot xH_2O$ (Aldrich). Catalysts were dried in air at 380 K overnight, followed by calcination at 538 K (1 K min^{-1} ramp) in flowing air (250 cm^3 (STP) min^{-1}) for 2 h. The dispersions of Pd on SBA-15-ALD-19 and HY-340 samples were 19% and 15%, respectively.

2.4. Characterization Methods. XRD analyses were carried out using a Siemens STOE diffractometer (Cu Kα, λ = 1.5406 Å) at 25 mA and 40 kV. Diffraction patterns were collected in a continuous mode with a step width of 0.02° and with an acquisition time of 10 s per step. Samples were examined by STEM in a JEOL 2010F microscope. The powders were deposited on holey carbon support films after being dispersed in ethanol. An electron probe, diameter of 0.2 nm, was scanned over the specimen, and electrons scattered at high angles were collected to form the images. The image contrast in the HAADF (high angle annular dark field) mode is atomic-number-dependent and is dependent also on the sample thickness in each pixel being imaged.

Raman spectra were recorded using an excitation wavelength of 532 nm on a LabRAM Aramis Horiba Jobin Yvon confocal Raman microscope. Spectra of compressed pellets of the samples were collected under hydrated conditions at room temperature. Nitrogen adsorption−desorption isotherms were measured at 77 K using a Micromeritics ASAP 2020 system. The samples were pretreated under vacuum at 393 K for 12 h. Surface areas were determined using the BET method. Pore size distribution data were collected by the BJH method of the desorption branch of the isotherm.

Pore volumes were determined from the adsorption branch of the N_2 isotherm at P/P_0 = 0.97 single point. The niobium content of each sample was measured by inductively coupled plasma-atomic emission spectrometry (ICP) analysis using a Perkin-Elmer Plasma 400 ICP emission spectrometer after dissolving the sample in HF.

The consumption of surface silanol groups on SBA-15-ALD-y catalyst was monitored by FTIR spectroscopy. The presence of niobia hydroxyl groups was also monitored by FTIR spectroscopy for niobia, HY-340, and SBA-15-ALD-30. Approximately 5−10 mg of self-supported sample was pelletized (∼1 cm^2) and treated in an IR cell where the samples were heated to 673 K for 2 h to remove adsorbed water from the surface under flowing He prior to measurements.

For FTIR experiments to probe hydroxyl groups on niobia, samples of HY-340 and SBA-15-ALD-30 were treated at both 473 and 673 K for 2 h in an IR cell under flowing He prior to measurements. The cell was cooled to room temperature and placed in the infrared spectrometer. Spectra were collected in the absorbance mode in a Mattson Galaxy Series 3000 FTIR, and spectra were normalized by the density of the sample pellet. Temperature-programmed desorption of NH_3 was used to measure the total numbers of acid sites of SBA-15-ALD-y samples by loading (∼100 mg) catalyst in a glass flow-through cell. NH_3 was adsorbed on the sample by exposure to a flowing gas mixture of 1 mol % NH_3 in He (100 cm^3 (STP) min^{-1}) at 423 K for 45 min. Residual ammonia was desorbed at 423 K with a He purge (150 cm^3 (STP) min^{-1}). Temperature-programmed desorption was performed using a temperature ramp of 10 K min^{-1} from room temperature to 1073 K under flowing He (50 cm^3 (STP) min^{-1}), and NH_3 desorption was quantified by an online mass spectrometer. Measurements of CO chemisorption on 1 wt % Pd-supported niobia catalysts were carried out using a Micromeritics ASAP 2020 system. Prior to measurements, catalysts were reduced in flowing H_2 for 3 h at 538 K (1.5 K min^{-1}) and purged for 1 h with ultrahigh purity He (200 cm^3 (STP) min^{-1}) at 538 K. Catalysts were cooled to 300 K, followed by subsequent dosing of CO. The gas phase was then evacuated for 1 h, and a second isotherm was collected, and the irreversible CO uptake was determined by subtracting the two isotherms. Pd dispersions were calculated on the basis of a Pd/CO stoichiometry of 2:1.

2.5. Hydrothermal Treatments. Hydrothermal treatments of HY-340, SBA-15, and SBA-15-ALD-y materials were carried out by adding 0.3 g of solid and 14 mL of water in a 50 mL pressure vessel (model 4792, Parr Instrument). The vessel was pressurized with 28 bars of argon, followed by heating to 473 K and holding at this temperature for 12 h. The treated samples were then washed with water, filtered, and dried in an oven at 393 K overnight.

2.6. Catalytic Activity Measurements. Studies of 2-propanol dehydration were carried out at 453 K and atmospheric pressure in a fixed-bed up-flow reactor. The reactor setup consisted of a 1/4-in.-o.d. stainless steel tubular reactor containing 100 mg of catalyst. An HPLC pump (Lab Alliance Series 1) was used to feed 2-propanol (Aldrich) to the reactor at a WHSV of 15 h^{-1}along with a cofeed of He at a rate of 20 cm^3 (STP) min^{-1}. Liquid effluents were collected in a liquid−gas separator at room temperature and drained for chromatographic analysis (Shimadzu GC-2010 with FID detector). The effluent gas was analyzed with an online GC (Varian GC, Saturn 3) using an FID detector and GS-Q capillary column (J & W Scientific). Overall total carbon balance closed within ±10%.

Reaction kinetics studies for the dehydration of 2-butanol were conducted in a fixed-bed up-flow reactor containing 100 mg of catalyst mixed with silica chips in a 1/4-in.-o.d. stainless steel tube. The reactor was held at a temperature of 513 K and a system pressure of 51 bar. A mass flow controller Brooks model 5850 was used to control the sparging gas flow to the reactor and, therefore, to control the concentration of water in the reactor. Prior to reaction kinetic measurements, the reactor was pressurized to 51 bar and heated to 513 K while flowing sparging gas (He) at a flow rate of ∼250 cm^3 (STP) min^{-1}. After flowing He for 1 h at the reaction temperature and pressure, a liquid feed consisting of 10 wt % 2-butanol in water mixture was pumped into the reactor at a rate of 0.1 cm^3 min^{-1} by an HPLC pump (Lab Alliance Series 1) along with a cofeed of helium as the sparging gas at a flow rate between 0 and 250 cm^3 (STP) min^{-1}. For each sparging gas flow rate, the system was allowed to stabilize for a minimum of 6 h to reach steady state before sampling the effluent gas and liquid phases for analysis. Major products detected for a typical run were the intramolecular dehydration products 1-butene, cis-2-butene, and trans-2-butene, with total carbon balances closing within 5% for each point taken. Liquid effluents were collected in a liquid−gas separator at room temperature and drained for chromatographic analysis (Shimadzu GC-2010 with FID detector). The effluent gas was analyzed with an online GC (Varian GC, Saturn 3) using an FID and GS-Q capillary column (J & W Scientific). For low sparging gas flow rates, an additional sweep gas was introduced in the liquid−gas separator to carry gaseous products from the reaction to the online GC for analysis.

Reaction studies to convert γ-valerolactone (GVL) to pentanoic acid were conducted at 573 K and 35 bar in an up-flow tubular reactor. A detailed description of the apparatus is given elsewhere.[35] Before reaction kinetics measurements, the catalyst was reduced at 538 K under flowing H_2 (100 cm^3 (STP) min^{-1}) for 3 h. A feed composed of 50 wt % GVL in water and a cofeed of H_2 and He (each 25 cm^3 (STP) min^{-1}) were used to provide a H_2 to GVL molar ratio of 2.2. WHSV was calculated on the basis of the GVL mass. Liquid effluents were collected in a liquid−gas separator at room temperature, and compositions were quantified in a Waters 2695 HPLC system equipped with RI 410 refractive index and PDA 960 UV detectors. The consumption of GVL was monitored with an Aminex HPX-87P (Bio-Rad) column at a temperature of 358 K using Milli-Q (pH 7) water as the mobile phase at 0.6 cm^3 min^{-1}. The production of pentanoic acid was monitored with an Aminex HPX-87H (Bio-Rad) column at 353 K using Milli-Q (pH 2) water as the mobile phase at 0.6 cm^3 min^{-1}. The effluent gas stream was analyzed with an online GC (Varian GC, Saturn 3) using an FID and GS-Q capillary column (J & W Scientific). CO_2 was analyzed with a Carle GC (series 400 AGC) using a TCD and a Q column (Porpak).

3. RESULTS AND DISCUSSION

3.1. Synthesis of Mesoporous Niobia by ALD. In the first step of niobia ALD, $Nb(OCH_2CH_3)_5$ reacts with hydroxyl groups on the surface, producing a grafted $Nb(OCH_2CH_3)_x$ surface species (with $x \sim 4$) and releasing approximately one ethoxy ligand in the form of ethanol. In the second step, H_2O hydrolyzes the remaining ethoxide ligands, releasing them as ethanol and repopulating the niobia surface with hydroxyl groups.[36,37] The surface coverage resulting from a single ALD cycle on a high-surface-area, nanoporous support depends on a number of kinetic, geometric, and thermodyamic parameters, including (i) the ALD conditions used (temperature, flow, time of exposure); (ii) the reactivity of the metal precursor toward the support surface; (iii) the diffusion coefficient and size of the precursor molecule; (iv) the surface area, particle size, and pore size of the support; and (v) the maximum growth per cycle that is dictated by the

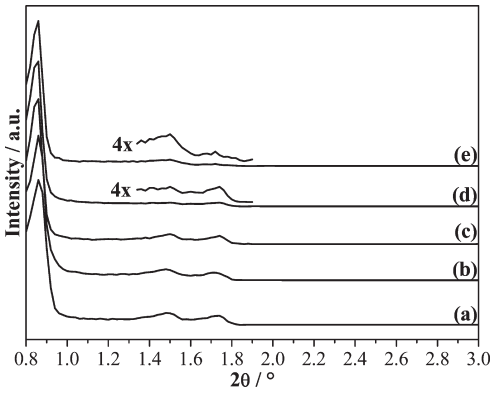

Figure 1. X-ray diffraction for (a) SBA-15, (b) SBA-15-ALD-1, (c) SBA-15-ALD-10, (d) SBA-15-ALD-19, and (e) SBA-15-ALD-30.

density of reactive surface sites and the projected size of the grafted metal precursor.[38] Consequently, it is important to establish the number of niobia ALD cycles required to form a coherent layer. For the samples prepared in this manuscript, preliminary studies were performed to establish the necessary saturation exposure conditions and to ensure that the niobia loadings were not limited by kinetics or substrate geometry. Nevertheless, these conditions do not guarantee that the silica surface becomes completely coated following a single niobia ALD cycle. Indeed, previous studies have shown that multiple cycles are typically required to form a coherent layer on the support surface because the growth per cycle is often a fraction of the monolayer thickness and because the precursor adsorption sites can sometimes be random.[39−41] In the present study, we varied the thickness of the niobia layer on SBA-15 by adjusting the number of deposition cycles, and these samples are denoted as SBA-15-ALD-*y*, where *y* corresponds to the number of cycles deposited (1, 10, 19, and 30). The structural properties, stabilities, and catalytic activities of these materials are discussed below.

XRD patterns were collected to confirm the initial formation of the SBA-15 structure and to study the stability of this structure after ALD cycles (Figure 1). The structure of SBA-15 displays hexagonal *P6mm* symmetry, and thus, three characteristic XRD peaks due to the (100) (most intense), (110), and (200) Miller indices are expected at relative 2θ values of X, $(\sqrt{3})X$, and $2X$, respectively.[42] The XRD pattern of the SBA-15 synthesized in this work (Figure 1a) showed all three expected peaks, confirming the formation of the structure. Importantly, after the ALD cycles, the same XRD pattern (Figure 1b−e) and unit cell parameter were found (a_0 = 11.85 nm), calculated from the (100) XRD peak using the equation $a_0 = \lambda/(\sqrt{3}\sin\theta)$.[43] However, the relative intensities of the (110) and (200) peaks with respect to the (100) peak decrease, mainly for SBA-15-ALD-19 and SBA-15-ALD-30, due to the formation of niobia layers over the silica walls. Schüth and co-workers[44] reported that for materials with the same unit cell parameter, increasing wall thickness leads to a decrease in the relative intensity of the (110) and (200) peaks. No further XRD peaks were observed for SBA-15 or SBA-15-ALD samples at $2\theta > 3°$, indicating that no crystalline phase was formed.

Dark-field STEM images of SBA-15-ALD-*y* materials were obtained to monitor the deposition of niobia within the mesopores of SBA-15 (Figure 2). Bright areas in the STEM image show the pore walls and the niobia coating, and the dark lines represent the empty pore space. For all samples, the organization of the channels is clearly shown, confirming the XRD results. High magnification STEM images of SBA-15 and SBA-15-ALD-30 are shown in Figure 3. The high-angle annular dark field images show the pore walls as bright regions and the pores as darker regions. In Figure 3A, the silica wall of SBA-15-ALD-30 can be differentiated from the niobia coating. The thin dark lines sandwiched between the brighter lines represent the silica walls that have been coated by niobia. Since STEM is based on *Z* contrast (atomic number) and niobia is heavier than silica, the niobia layers appear brighter than the silica walls shown in Figure 3A. In part B, this thin line is not seen in uncoated SBA-15.

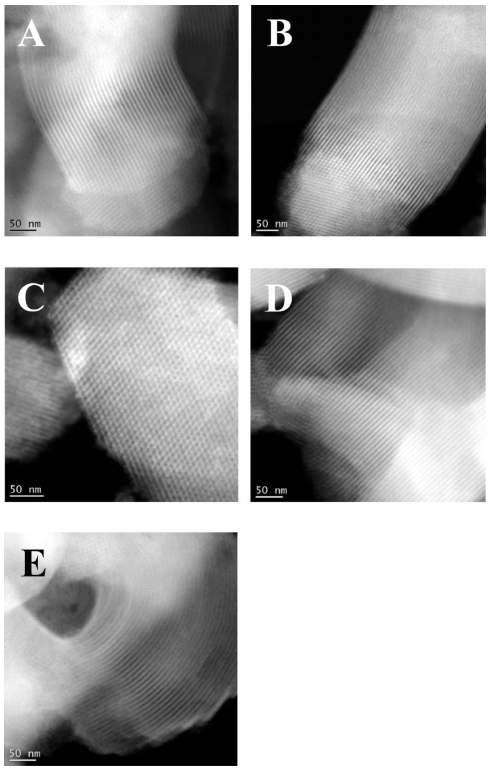

Figure 2. Dark-field STEM images of (A) SBA-15, (B) SBA-15-ALD-1, (C) SBA-15-ALD-10, (D) SBA-15-ALD-19, and (E) SBA-15-ALD-30.

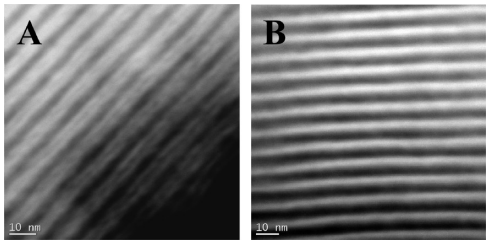

Figure 3. High-magnification STEM images of (A) SBA-15-ALD-30 and (B) SBA-15.

To determine the number of ALD cycles needed for complete coverage of the silica surface, FTIR was used to monitor the progressive consumption of surface silanol groups after 1, 10, 19, and 30 ALD cycles (Figure 4). In the region between 3800 and 3600 cm^{-1}, the FTIR spectrum of SBA-15 (Figure 4a) is characterized by a band at 3743 cm^{-1} due to isolated silanol groups and

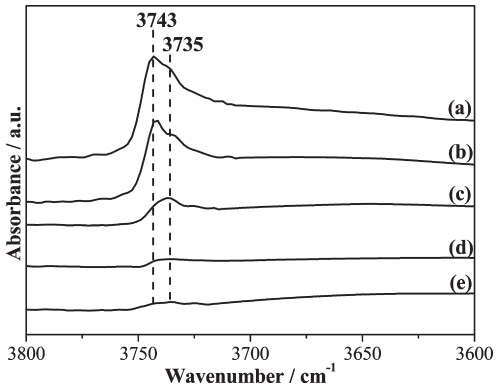

Figure 4. FTIR spectra of (a) SBA-15, (b) SBA-15-ALD-1, (c) SBA-15-ALD-10, (d) SBA-15-ALD-19, and (e) SBA-15-ALD-30.

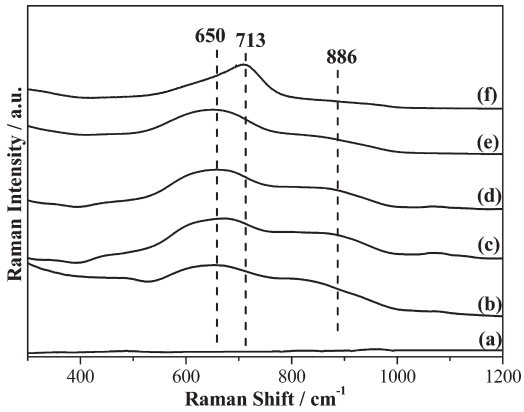

Figure 5. Raman spectra of (a) SBA-15, (b) SBA-15-ALD-10, (c) SBA-15-ALD-19, (d) SBA-15-ALD-30, (e) amorphous bulk niobia HY-340, and (f) crystalline bulk niobia HY-340 (TT-phase).

a band at 3735 cm^{-1} attributed to weakly perturbed silanol groups.[45] A small decrease in the silanol bands is observed in the spectrum for SBA-15-ALD-1 (Figure 4b) due to reaction of these groups with the niobium precursor. After 10 ALD cycles (Figure 4c), almost all the silanol groups have reacted. At this point, it is possible that a monolayer of niobium oxide is formed and that the remaining silanols could be located in the defects of this monolayer. The silanol band decreases further after 19 ALD cycles (Figure 4d). The remaining silanol groups are probably unavailable for reaction (in blocked defects or micropores) because no additional decrease in the surface silanol IR band is observed in the sample after 30 ALD cycles (Figure 4e). Attempts to definitively observe the band for hydroxyl groups associated with niobia for SBA-15-ALD-*y* samples were ambiguous due to the intensity of the bands associated with the remaining unreacted silanol species (Supporting Information, Figures S1−S3).

Raman spectroscopy was employed to probe the nature of the metal oxide species created on the surface of SBA-15 and to compare these species with those found in amorphous and crystalline niobia (Figure 5). The spectrum for amorphous bulk niobia displays bands at 650 and 886 cm^{-1}, as shown in Figure 5e. The first band is attributed to the symmetric stretching mode of slightly distorted NbO_6, NbO_7, and NbO_8 species.[46,47] Wachs and co-workers[48] studied niobia supported on different metal oxides and reported that the band at 650 cm^{-1} appears only in highly polymerized niobium oxide, in which the metallic center is in a six-coordination environment. In hydrated niobia, the broad band at ∼886 cm^{-1} is assigned to Nb═O groups on a hydrated surface.[46,47] Because of the increasing bond order of the niobia polyhedra for crystalline bulk niobia (TT-phase), a shift of the Raman band was observed from ∼650 cm^{-1} (for the amorphous niobia) to ∼713 cm^{-1} (Figure 5f).[46,47] Only two Raman bands characteristic of amorphous bulk niobia (at ∼650 and ∼886 cm^{-1}) were observed for the samples obtained by 10, 19, and 30 ALD cycles (Figure 5b−d). In the case of SBA-15-ALD-1, no Raman bands were observed as a result of the low niobia loading (not shown).[22] As expected, SBA-15 did not show any Raman bands at 650 or 886 cm^{-1} (Figure 5a).[24] It can be concluded from these results that the niobia layers formed on the SBA-15-ALD-10, SBA-15-ALD-19, and SBA-15-ALD-30 are structurally similar to bulk hydrated amorphous niobia (HY-340).

Measurements of N_2 physisorption were conducted to monitor the evolving structural properties of SBA-15-ALD-*y* materials at various niobia loadings. Table 1 summarizes the compositional and structural properties of these materials. Isotherms of SBA-15 and SBA-15-ALD-*y* are shown in Figure 6. SBA-15 presents a type-IV isotherm (Figure 6, curve a), as expected for this mesoporous silica.[32] The adsorption branch is characterized by two steps: (i) the formation of a nitrogen monolayer and the filling of the micropores at $P/P_0 < 0.1$ and (ii) capillary condensation in the mesopores at $0.6 < P/P_0 < 0.9$.[49] In the desorption branch, the presence of an H1 hysteresis loop is indicative of the predominance of well-defined cylindrical pores.[49] The isotherms for the SBA-15-ALD-1, SBA-15-ALD-10, and SBA-15-ALD-19 samples (Figure 6, curves b, c, and d) are similar in shape to the isotherm obtained for pure silica SBA-15 but with a lower volume of nitrogen physisorbed, which decreases with increasing niobia loading. The conservation of the H1 hysteresis loop indicates that the mesopores are still uniform and cylindrical after the deposition of niobia layers without pore blocking.[21] The SBA-15-ALD-30 sample displayed a type-IV isotherm but exhibited an H2 hysteresis loop for the desorption branch, indicating irregularly shaped pores due to niobia particulates dispersed within the mesopores.[49]

Applying the BJH model to the desorption branch of the nitrogen isotherms, we determined the pore diameters of SBA-15 and the SBA-15-ALD-*y* materials; pore size distribution (PSD) curves are shown in Figure 7. SBA-15 initially has a pore diameter of 6.49 nm, and this value decreases upon the deposition of niobia layers. For SBA-15 deposited with 1 ALD cycle, a reduction of the pore size to 5.80 nm was observed. Considering the low loading of niobia and the incomplete coverage of the surface, such a sizable reduction of pore diameter was not expected. Even though the use of the desorption branch to calculate the pore diameter is recommended when the isotherm hysteresis is H1,[49−51] the BJH model applied to the desorption branch of the isotherm can lead to an artificial narrowing of the PSD for materials with nonuniform coverage of the surface (such as SBA-15-ALD-1).[52] This finding is confirmed in Figure 7, where the PSD for SBA-15-ALD-1 (full square in the figure) is inside the range of PSD for SBA-15 (open square in the figure), but significantly narrower. For SBA-15-ALD-10, the pore diameter was 5.60 nm, which suggests an increase of 0.89 nm in the SBA-15 wall thickness due to the niobia layer.

According to previous studies,[53,54] the density of niobium atoms in a monolayer covering amorphous silica is 6.3 niobium atoms/nm^2. For SBA-15-ALD-10, it was determined that the density of the deposited layer is 6.4 niobium atoms/nm^2. Shirai, et al.[55] studied the niobium oxide bond on a silica surface and determined bond lengths for the species at the interface between

Table 1. Chemical Composition, Surface Area and Porosity Properties of SBA-15 and SBA-15-ALD-*y* Materials

sample	Nb_2O_5[a] (mol %)	S_{BET}[b] (m^2g^{-1})	expected S_{BET}[c] (m^2g^{-1})	S_{microp}[d] (m^2g^{-1})	V_P (cm^3g^{-1})	$V_{P\text{-}microp}$[d] (cm^3g^{-1})	D_P[e] (nm)	W[f] (nm)	Nb_2O_5 thickness (nm)
HY-340	100	118							
SBA-15		930	930	162	1.11	0.078	6.49	5.36	
SBA-15-ALD-1	3.3	671	687	90	0.78	0.034	5.80	6.05	0.35
SBA-15-ALD-10	16.8	326	351	0	0.46	0	5.60	6.25	0.45
SBA-15-ALD-19	22.2	246	247	0	0.32	0	4.75	7.10	0.87
SBA-15-ALD-30	32.3	126	142	0	0.14	0	3.74	8.11	1.38

[a] Determined by ICP analysis. [b] BET specific surface area. [c] Expected BET specific surface area based on the measured weight gain and reduction of pore diameter as niobia is deposited. [d] Micropore surface area and volume determined by the *t*-plot method. [e] Calculated by BJH method. [f] Wall thickness determined by $a_0 - D_P$.

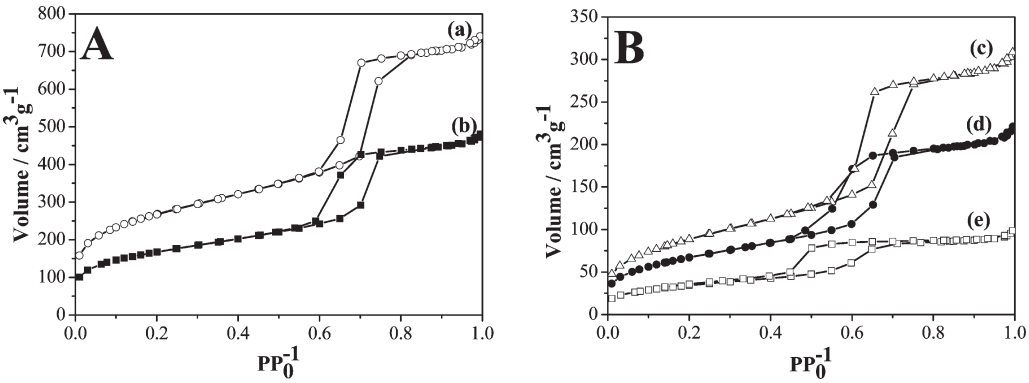

Figure 6. Nitrogen physisorption isotherms at 77 K for (A) SBA-15 (a), SBA-15-ALD-1 (b); (B) SBA-15-ALD-10 (c), SBA-15-ALD-19 (d), and SBA-15-ALD-30 (e).

the silica and the niobium oxide. According to the bond length values, a monolayer of niobia would have a thickness of ~0.4 nm, and hence, for a monolayer of niobia in a SBA-15 channel, this would suggest a reduction of 0.8 nm in the pore diameter. Furthermore, Du, et al.[24] estimated a 0.7 nm increase in the wall thickness due to the formation of a monolayer of vanadium oxide grafted on SBA-15. This value is relatively close to the one found for SBA-15-ALD-10, considering the difference in the bond length and in the methods used for pore size determination. Thus, we conclude that a complete monolayer of niobia was formed for the SBA-15-ALD-10 sample. For SBA-15-ALD-19 and SBA-15-ALD-30, the pore diameters were 4.75 and 3.74 nm, respectively. The niobia layer thicknesses for these materials correspond to 0.87 and 1.38 nm, representing the deposition of 2 and 3 monolayers, respectively. Therefore, under the ALD conditions used for the synthesis of SBA-15-ALD-*y* materials, approximately each 10 ALD cycles produces one monolayer of niobia.

As summarized in Table 1, the deposition of niobia layers within the pores of SBA-15 leads to significant reduction in the micropore surface area, overall surface area, and pore volumes. To correlate the reduction in pore size to that of the surface area, the expected surface areas after the niobia depositions were calculated on the basis of the decrease in mesopore diameter, the loading of niobia, and considering micropore blockage. The values obtained are in good agreement with experimental measurements (Table 1). Surface area reductions of the same magnitude have been observed for zirconia,[21] titanium phosphate,[28] or manganese oxide[56] grafting on SBA-15.

Niobium oxide in its hydrated form (also called niobic acid) is known to be a solid acid catalyst for several reactions.[5] To probe

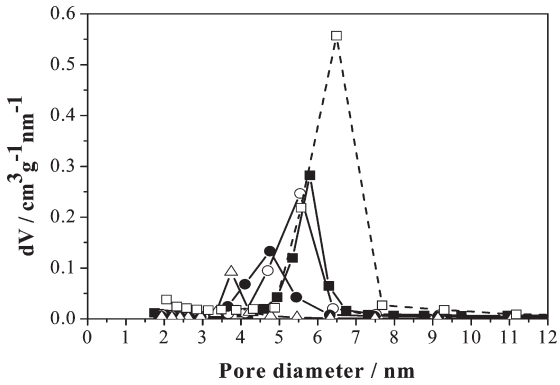

Figure 7. Pore size distribution for (□) SBA-15, (■) SBA-15-ALD-1, (○) SBA-15-ALD-10, (●) SBA-15-ALD-19, and (Δ) SBA-15-ALD-30.

the acidic properties of the niobia layer deposited, the total number of surface acid sites for the ALD-prepared materials was quantified by NH_3−TPD and compared with bulk niobia (HY-340), as shown in Table 2. The SBA-15-ALD-1 sample, in which the surface is only partially covered, has an acid site density of 152 μmol g^{-1}, compared wtih 132 μmol g^{-1} for HY-340. SBA-15-ALD-10 and SBA-15-ALD-19 contain ~2.5 times more acid sites per unit mass of material. However, for both samples, the acid site densities normalized by their respective surface areas are comparable to HY-340. This observation is consistent with the conclusion that complete coverage of the silica surface with niobia has been achieved for these samples, leading to a surface-weighed acid site density similar to that

Table 2. Total Acid Site Density of Bulk Niobia, HY-340, and SBA-15-ALD-*y* Measured by NH_3 TPD

catalyst	total acid sites	
	μmol g^{-1}	μmol m^{-2}
HY-340	132	1.1
SBA-15-ALD-1	152	0.2
SBA-15-ALD-10	345	1.1
SBA-15-ALD-19	325	1.3
SBA-15-ALD-30	226	1.8

of HY-340. The highest apparent concentration of acid sites per area (1.8 μmol m^{-2}) was found on SBA-15-ALD-30. This anomaly may be explained by the underestimation of the surface area due to the presence of niobia particulates, as indicated by the distinctive shape of the nitrogen isotherm.

From the physical properties presented above, the materials synthesized by ALD combine the highly ordered porous structure of SBA-15 with the surface properties of niobia and can be considered as a new class of mesoporous niobia.

3.2. Hydrothermal Stability of Mesoporous Niobia. The hydrothermal stabilities of SBA-15 and the SBA-15-ALD-*y* samples were studied by treating these materials in liquid water for 12 h at 473 K (pressurized with 28 bar of Ar in the batch reactor). XRD patterns of hydrothermally treated materials are shown in Figure 8. The XRD pattern of SBA-15 (Figure 8a) does not show any peaks after the hydrothermal treatment, indicating complete collapse of the hexagonal mesoporous structure. Comparison of the XRD patterns of SBA-15-ALD-*y* materials before (Figure 1b−e) and after (Figure 8b−e) the hydrothermal treatments shows that the XRD peaks were maintained, as well as the 2θ position of the (100) peak. Hence, for the SBA-15-ALD-*y* materials, the structural organization of the pores and the unit cell parameter were not appreciably changed. Wide-angle XRD patterns for SBA-15-ALD-19 are representative of those obtained for SBA-15-ALD-*y* materials, (Supporting Information, Figure S4). No peaks were observed at 2θ higher than 3°, and thus, no crystalline phase was formed during the hydrothermal treatment. This behavior is in contrast to bulk niobia, HY-340, which transforms to a highly crystalline material when treated at 473 K in water with a corresponding decrease in surface area from 118 to 17 m^2 g^{-1}.

TEM images for all samples after the hydrothermal treatment are shown in Figure 9. In agreement with the XRD results, the collapse of SBA-15 structure (Figure 9A) shown in the TEM images demonstrates the low hydrothermal stability of the pure silica molecular sieve. For SBA-15-ALD-1, a combination of particles with partially collapsed (Figure 9B) and particles with organized pore structure (Figure 9B′) was observed. It is clear that for this material, niobia partially protects the structure from hydrolytic cleavage. For the materials prepared by 10, 19, and 30 cycles (Figure 9C, D, and E, respectively), well-organized porous structures were observed after the treatment, confirming the remarkable hydrothermal stability of the niobia-coated mesoporous materials prepared.

Measurements of N_2 physisorption were carried out on SBA-15-ALD-*y* samples to provide further evidence regarding their hydrothermal stability, as shown in Table 3 and Figure 10. In particular, no substantial changes in the structural properties, pore sizes, and surface areas were observed for SBA-15-ALD-10,

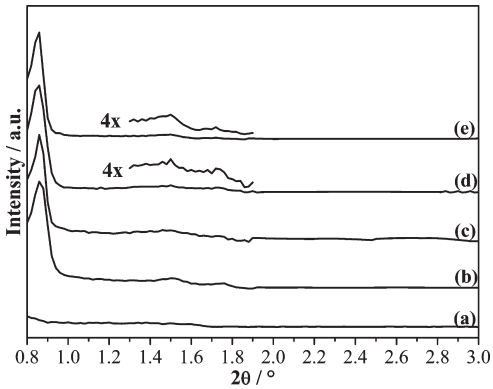

Figure 8. X-ray diffraction for (a) SBA-15, (b) SBA-15-ALD-1, (c) SBA-15-ALD-10, (d) SBA-15-ALD-19, and (e) SBA-15-ALD-30 after hydrothermal treatment at 473 K.

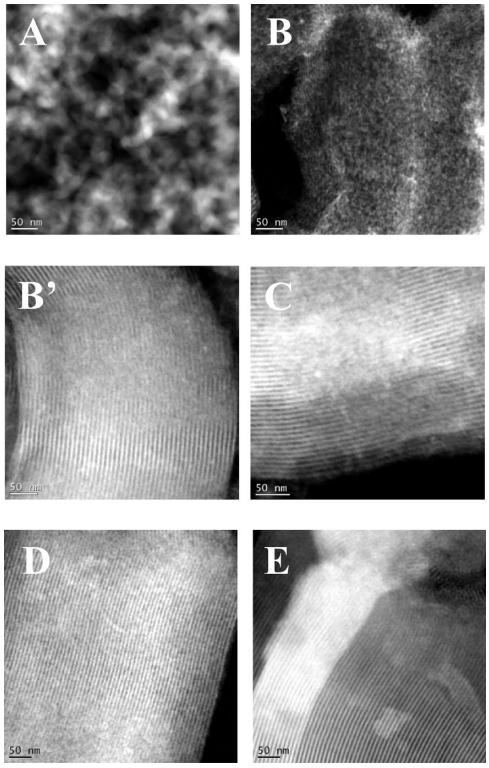

Figure 9. Dark-field STEM images of (A) SBA-15, (B, B′) SBA-15-ALD-1, (C) SBA-15-ALD-10, (D) SBA-15-ALD-19, and (E) SBA-15-ALD-30 after hydrothermal treatment at 473 K.

19, and 30 after hydrothermal treatment. In contrast, the surface area and porosity changed significantly for the SBA-15-ALD-1 sample where the silica scaffold is only partially coated with niobia (see Figures 6 and 7, and Table 1 for the results before hydrothermal treatment).

Hydrothermal treatment caused the surface area of SBA-15-ALD-1 to decrease by ∼50% due to partial collapse of the structure. In the nitrogen isotherm (Figure 10b), the occurrence of broad capillary condensation indicates the presence of a secondary family of mesopores. The PSD (Figure 11) shows two broad families of pores with maxima at 5.40 and 8.30 nm. The former peak represents the structural pores, which are reduced by 0.4 nm with respect to the original material (Table 1). The latter peak

Table 3. Surface Area and Porosity Properties of SBA-15 and ALD Modified SBA-15 after Hydrothermal Treatment at 473 K

sample	S_{BET}[a] (m^2g^{-1})	S_{Microp}[b] (m^2g^{-1})	V_P (cm^3g^{-1})	$V_{P\text{-}Microp}$[b] (cm^3g^{-1})	D_P[c] (nm)
HY-340	17				
SBA-15	31		0.09		
SBA-15-ALD-1	327	50	0.67	0.02	5.40/8.30
SBA-15-ALD-10	261	29	0.43	0.01	5.40
SBA-15-ALD-19	255	0	0.36	0	4.75
SBA-15-ALD-30	158	0	0.18	0	3.66

[a] BET specific surface area. [b] Micropore surface area and volume determined by the *t*-plot method. [c] Calculated by the BJH method.

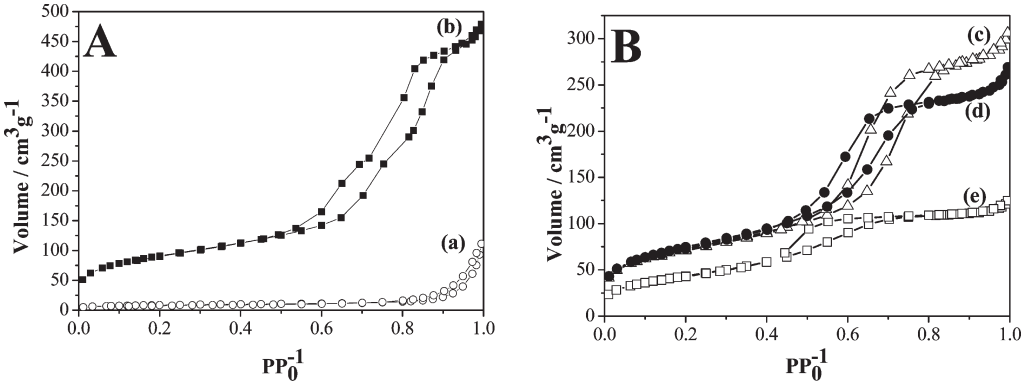

Figure 10. Nitrogen physisorption isotherms at 77 K of (A) SBA-15 (a), SBA-15-ALD-1 (b) and (B) SBA-15-ALD-10 (c), SBA-15-ALD-19 (d), and SBA-15-ALD-30 (e) after hydrothermal treatment at 473 K.

has a wide distribution between 8 and 14 nm. Considering that the unit cell parameter is 11.85 nm, these pores cannot be structural, and hence, they are attributed to interstitial spaces between the silica particles generated by the partial amorphization of the structure.[49]

Hydrothermal treatment caused a reduction of 20% in the specific surface area of SBA-15-ALD-10. On the basis of FTIR results for SBA-15-ALD-10, the remaining silanol groups located at the defects of the niobia monolayer can be potentially attacked by water, causing the reduction in surface area. A slight increase in microporosity was also observed that could be generated by water hydrolysis on these defects. For SBA-15-ALD-19, the PSD became slightly broader after treatment in water, and no other significant change took place. For SBA-ALD-30, a small increase in the surface area was observed, accompanied by a change in the hysteresis loop from H2 to H1, possibly due to the removal of discrete niobia particulates from the pores.

Treatment of SBA-15 in liquid water leads to a collapse of its hexagonal structure and mesoporosity (Figure 9a). In addition, the phase of bulk niobia transforms under hydrothermal treatment from amorphous to crystalline, accompanied by a significant reduction in surface area. In contrast, the coating of SBA-15 with niobia by ALD imparts remarkable hydrothermal stability to the resultant composite materials. The improved stability can be attributed to the formation of Nb−O−Si linkages during the reaction between surface silanols and the niobium precursor. The consumption of these silanol groups prevents hydrolytic cleavage of silica and, thus, the collapse of the framework.[57,58] The formation of Nb−O−Si linkages also stabilizes the niobia layer deposited and prevents it from undergoing phase transformation, as previously reported by Weissman, et al.[59]

On the basis of the experimental results compiled for SBA-15-ALD-*y* materials, SBA-15-ALD-19 possesses the mesoporous

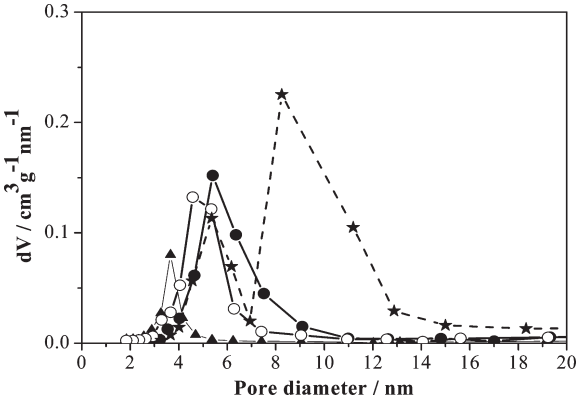

Figure 11. Pore size distribution for (★) SBA-15-ALD-1, (●) SBA-15-ALD-10, (○) SBA-15-ALD-19, and (▲) SBA-15-ALD-30 after hydrothermal treatment at 473 K.

structure of SBA-15, complete coverage of the surface silanol groups by niobia, acid site densities comparable to HY-340, and remarkable hydrothermal stability. Therefore, this SBA-15-ALD-19 material was used for reaction kinetic studies to probe its activity as a solid acid catalyst and as a support for metal nanoparticles, with emphasis on the stability of this material under reaction conditions relevant for the aqueous-phase processing of biomass derived molecules at high temperature and pressures.

3.3. Catalytic Properties of Mesoporous Niobia. *3.3.1. 2-Propanol Dehydration.* Vapor-phase dehydration of 2-propanol has been used extensively as a reaction to probe the nature of active sites (i.e., acidic, basic, or amphoteric) present on the surface of a wide range of solid catalysts,[60−62] including niobia,[60,63,64] based on the observed

product distribution. It has been demonstrated that niobic acid, which exhibits primarily acidic properties under the typical reaction conditions of 2-propanol dehydration (~423−523 K), produces propylene almost exclusively (selectivity >97%).[60,64] SBA-15-ALD-19 possesses surface species that have similar structure as well as comparable surface-weighed acid site density compared with bulk amorphous niobia, HY-340, as suggested by the results from Raman spectroscopy and NH_3−TPD, respectively. Therefore, one would expect similar reactivity and selectivity for 2-propanol dehydration between the two materials.

The catalytic properties of SBA-15-ALD-19 and HY-340 as-synthesized and after treatment in liquid water at 473 K for 12 h were compared in the dehydration of 2-propanol at 453 K and atmospheric pressure. SBA-15 did not show measurable catalytic activity for this reaction. For SBA-15-ALD-19 and HY-340, propylene was the only product detected in the outlet stream, which suggests the presence of active sites of similar nature in both materials. Rates for the dehydration of 2-propanol on these samples are listed in Table 4. In accordance with the difference in surface areas, the rate per catalyst mass was initially 3 times higher for SBA-15-ALD-19 compared with HY-340. After the hydrothermal treatment, SBA-15-ALD-19 showed comparable propylene formation rates before and after hydrothermal treatment, with values of 370 and 347 μmol min^{-1} g^{-1}, respectively. In contrast, the rates for HY-340 decreased significantly after the water treatment, leading to rates of reaction per catalyst mass 12 times lower than the SBA-15-ALD-19. If normalized by surface area, the rates of propylene formation are similar for all materials (from 1.0 to 1.6 μmol min^{-1} m^{-2}).

Table 4. Reactivity for the Dehydration of 2-Propanol at 453 K over HY-340 and SBA-15-ALD-19 before and after Treatment in Liquid Water at 473 K for 12 h

catalyst	propylene formation rate	
	μmol min^{-1} g^{-1}	μmol min^{-1} m^{-2}
SBA-15[a]	0	0
HY-340[a]	114	1.0
HY-340[b]	28	1.6
SBA-15-ALD-19[a]	370	1.5
SBA-15-ALD-19[b]	347	1.4

[a] Before treatment in liquid water at 473 K for 12 h. [b] After treatment in liquid water at 473 K for 12 h.

3.3.2. 2-Butanol Dehydration. Biomass-derived molecules are highly oxygenated compounds, often with high solubilities in water, thus requiring aqueous-phase processing conditions for the selective removal of oxygen for the production of fuels or chemicals. A particularly attractive strategy for the deoxygenation of carbohydrates and sugar alcohols is the APDH scheme, in which a solid acid is used to catalyze the dehydration of oxygenated hydrocarbons, followed by hydrogenation to form alkyl species in the presence of a metal catalyst and hydrogen. In APDH processing, dehydration over solid acids has been shown by previous studies to be the rate-limiting step, on the basis of the observation that alkenes were not typically observed in the APDH products when Pt was supported on a solid acid, such as silica−alumina, and the observation that the production rates of alkenes over silica−alumina and alkanes over Pt/silica−alumina were the same under the reaction conditions employed.[4] Herein, we present a study of the dehydration of 2-butanol, a probe molecule, over mesoporous niobia SBA-15-ALD-19 over a wide range of water concentrations, especially in the presence of liquid water to determine its potential as a water-tolerant solid acid catalyst for the APDH reaction.

Both SBA-15-ALD-19 and HY-340 were studied under the same reaction conditions, consisting of a 10 wt % 2-butanol/water mixture fed at a flow rate of 0.1 mL min^{-1} at 513 K and 51 bar with a sparging gas flow between 0 and 250 cm^3 (STP) min^{-1}. The production rates of butene for both catalysts are shown in Figure 12. For both SBA-15-ALD-19 and HY-340, the products observed were 1-butene and *cis*- and *trans*-2-butene. At high inert gas flow rates (i.e., higher than 74 cm^3 (STP) min^{-1}), the rate of butene production increased with increasing inert gas flow, whereas the opposite trend was observed at inert gas flow rates lower than 74 cm^3 (STP) min^{-1}. In addition, it should be noted that for all sparging gas flow rates, the higher surface area of SBA-15-ALD-19 leads to ~7−10 times higher rates of butene production per catalyst mass in comparison with HY-340.

At 513 K, the vapor pressures of water and 2-butanol are 33.3 and 30.8 bar respectively; thus, water, without the presence of a sweep gas, should remain in the liquid phase under a total system pressure of 51 bar. It has been determined by West et al.[4] that for water−butanol mixtures, the presence of a sparging gas stream at flow rates above about 70 cm^3 (STP) min^{-1} leads to complete vaporization of water and butanol, whereas liquid water is present in vapor−liquid equilibrium at gas flow rates below about 70 cm^3 (STP) min^{-1}.

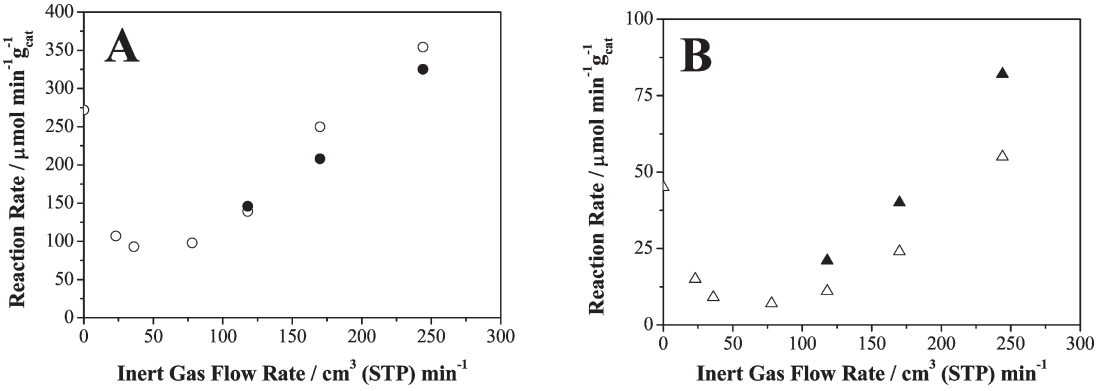

Figure 12. (A) Rate of butene production versus inert gas flow rate for (●) SBA-15-ALD-19 in the vapor regime and (○) SBA-15-ALD-19 after exposure to liquid water. (B) Rate of butene production versus inert gas flow rate for (▲) HY-340 in the vapor regime and (Δ) HY-340 after exposure to liquid water.

Kinetics models based on the combination of two adsorption mechanisms have been proposed by West et al.[4] to explain the effect of the inert gas flow rate on the rate of butene production. The first adsorption model is based on a Langmuir−Hinshelwood mechanism in which the 2-butanol dehydration reaction occurs between an adsorbed butanol molecule and a vacant site to produce adsorbed butene and adsorbed water. The second adsorption model invokes multilayer adsorption isotherms of various species, including the hydration of adsorbed butanol on the surface. Therefore, when the HY-340 and SBA-15-ALD-19 catalysts are initially exposed to the 10 wt % butanol water mixture in the vapor regime at a high sweep gas flow rate of ∼250 cm^3 (STP) min^{-1}, the rate of butene production is at its highest value, since the catalyst surface contains a high concentration of vacant sites for the surface reaction between adsorbed butanol and a vacant site. As the sweep gas flow rate decreases from 250 to 74 cm^3 (STP) min^{-1}, the partial pressure of water increases, the number of vacant sites decreases as these sites become occupied by adsorbed water, and the butene production rate decreases accordingly. As the inert sweep gas decreases further to flow rates below 74 cm^3 (STP) min^{-1}, the system transitions to the vapor−liquid regime, and the dominant surface reaction mechanism becomes the reaction between hydrated vacant sites and adsorbed hydrated butanol. As the inert gas flow rate decreases, a higher fraction of the volatile 2-butanol reactant remains in the liquid phase, and the rate of butene production increases accordingly.

After contacting the SBA-15-ALD-19 and HY-340 catalysts with liquid water at low sweep gas flow rates, the catalysts were then re-exposed to the vapor regime at higher gas sweep flow rates, and the rates of butene production were measured. It can be observed from Figure 12B that the rate of butene production for HY-340 showed a decrease in activity after exposure to liquid water, caused by the poor hydrothermal stability of this material in the presence of liquid water at temperatures above 473 K, as discussed previously. In contrast, similar butene production rates were observed when the SBA-15-ALD-19 catalyst was re-exposed to the vapor regime, shown in Figure 12A, demonstrating the superior stability of this catalyst, even after exposure to liquid water under aqueous phase processing conditions.

Scheme 1. Reaction Scheme for the Transformation of γ-Valerolactone to Pentanoic Acid[a]

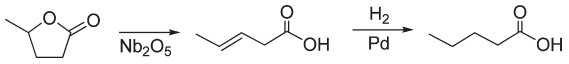

[a] Nb_2O_5 catalyzes the ring-opening of γ-valerolactone to pentenoic acid, followed by a metal catalyzed hydrogenation to pentanoic acid.

3.3.3. GVL Conversion to Pentanoic Acid. The conversion of GVL to pentanoic acid has recently been investigated in a number of promising biorefinery schemes.[65−67] This reaction occurs by an acid-catalyzed ring-opening step of GVL to pentenoic acid, followed by a metal-catalyzed hydrogenation step to pentanoic acid (Scheme 1).[68] We have previously studied this reaction over bifunctional catalysts consisting of Pd nanoparticles supported on commercial amorphous niobia (HY-340) and on niobia containing small amounts of silica in its framework.[12] It has been demonstrated that niobia, in its amorphous phase, not only provides the required acid functionality for the transformation, but also plays a critical role in maintaining the dispersion of Pd particles through the well-known strong metal−support interaction.[63] However, crystallization of niobia induces sintering and possible encapsulation of Pd particles, leading to loss of catalytic activity, as in the case of Pd supported on HY-340.[12] Given its acidity and remarkable hydrothermal stability demonstrated in previous sections, SBA-15-ALD-19 was further studied as a promising reactive support for bifunctional catalytic systems.

Reaction kinetics studies for the conversions of GVL to pentanoic acid were conducted at 573 K and 35 bar using 1 wt % Pd supported on SBA-15-ALD-19. Figure 13A shows the conversion of GVL versus time-on-stream for Pd impregnated on SBA-15-ALD-19 and on HY-340. In these experiments, pentanoic acid was obtained with >90% selectivity, and carbon balances closed within ±10%. Minor products detected were butane and CO_2. It is evident that the Pd/SBA-15-ALD-19 catalyst showed superior stability for at least 70 h of time-on-stream.

Deactivation rate constants were obtained from the data of Figure 13 to provide a quantitative comparison of the rate of deactivation between these two catalysts. The GVL conversion was modeled as a pseudo-first-order reaction, and the reactor, as an integral packed bed plug flow reactor. The decay in catalytic activity was described by a first-order exponential law. The deactivation rate constant, k_d, can be determined from the slope of the straight line when ln(k) is plotted against t, where k is the pseudo-first-order rate constant with units of mol h^{-1} atm^{-1} g_{cat}^{-1} and t represents time-on-stream in hours, as shown in Figure 13B. It can be seen from Figure 13B that Pd/HY-340 exhibited rapid

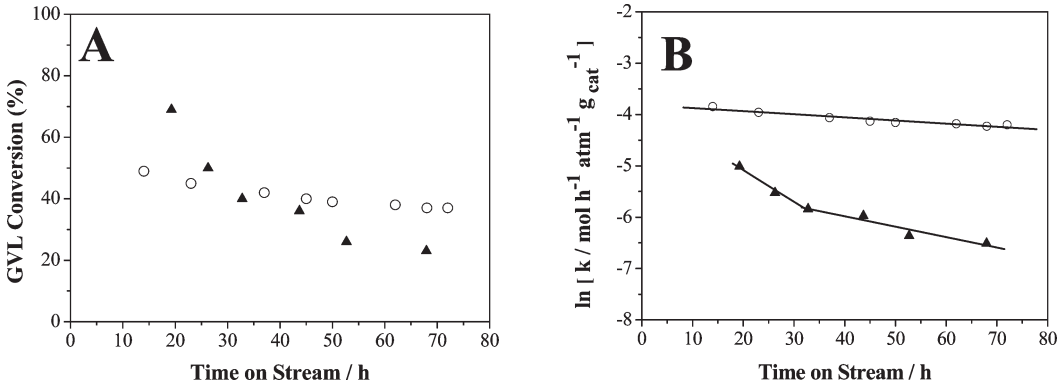

Figure 13. (A) GVL conversion as a function of time-on-stream for (▲) Pd/HY-340 at 573 K and 35 bar, WHSV 3 h^{-1} and (○) Pd/SBA-15-ALD-19 at 573 K and 35 bar, WHSV 17 h^{-1}. (B) Estimation of deactivation rate constants assuming pseudo-first-order reaction (with a rate constant, k) and first-order deactivation for (▲) Pd/HY-340 and (○) Pd/SBA-15-ALD-19.

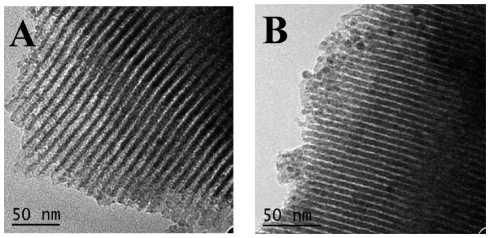

Figure 14. HRTEM images for Pd/SBA-15-ALD-19 (A) before (B) after GVL reaction.

deactivation during the initial 32 h on stream, followed by a stage in which the activity decreased less steeply. The values of deactivation constants for both stages are 0.0597 and 0.0203 h^{-1}, respectively. In contrast, the Pd/SBA-15-ALD-19 catalyst showed a substantially slower deactivation over the entire time-on-stream period investigated, giving a deactivation constant of 0.0061 h^{-1}.

To elucidate the superior stability of the Pd/SBA-15-ALD-19 catalyst, HRTEM images were taken before and after GVL reaction kinetic studies, with representative images shown in Figure 14. The observable Pd particle sizes in the HRTEM image for as-synthesized Pd/SBA-15-ALD-19 sample are ~1.5−2 nm, although there can be particles smaller than 1 nm not discernible by the image. After the GVL reaction, the HRTEM image for the Pd/SBA-15-ALD-19 sample shows a modest growth of the particles; however, most of the particles are still smaller than 5 nm. In addition, HRTEM images show that the integrity of the mesoporous structure of Pd/SBA-15-ALD-19 was retained after reaction conditions. In contrast, the catalyst consisting of Pd supported on HY-340, previously studied by Pham, et al.,[12] showed significant sintering of Pd, leading to particle sizes >10 nm after exposure to the same conditions, as well as the transformation of HY-340 from amorphous to the crystalline phase. Clearly, coating SBA-15 with niobia by atomic layer deposition has created a mesoporous niobia with superior hydrothermal stability that can be used as a catalyst support for the processing of biomass-derived compounds.

4. CONCLUSIONS

Highly ordered mesoporous niobia materials have been synthesized by atomic layer deposition. Analyses of N_2 adsorption−desorption isotherms indicated that layers of niobia (produced from 10, 19, and 30 ALD cycles) were deposited uniformly within the pores of SBA-15. These mesoporous niobia materials exhibited excellent stability in liquid water at temperatures up to 473 K, as evidenced by N_2 adsorption−desorption isotherms, STEM analyses, and XRD measurements. These materials showed high catalytic activity for the dehydration of 2-propanol and 2-butanol, even after exposure to liquid water at elevated temperatures and pressures. Furthermore, mesoporous niobia impregnated with Pd nanoparticles showed remarkable stability with time-on-stream in the catalytic conversion of GVL to pentanoic acid.

ALD offers great flexibility and degree of control over the composition of the oxides that can be deposited in mesoporous silica, with the potential to create new materials with controlled surface properties. These materials can serve as hydrothermally stable supports for metal nanoparticles or scaffolds for further anchoring of functional moieties on the deposited layers. The synthesis technique employed in this study can have important implications in the synthesis of mesoporous materials possessing the hydrothermal stability and catalytic properties necessary for the transformation of biorenewable molecules under aqueous conditions at elevated temperatures.

■ ASSOCIATED CONTENT

Supporting Information. FTIR spectra of the Nb−OH band region for HY-340 and SBA-15-ALD-30 pretreated at 473 and 673 K. XRD patterns of HY-340 and SBA-15-ALD-19 before and after hydrothermal treatment. This material is available free of charge via the Internet at http://pubs.acs.org.

■ AUTHOR INFORMATION

Corresponding Author

*Phone: +1 (608) 262-1095. Fax: +1 (608) 262-5434. E-mail: dumesic@engr.wisc.edu.

■ ACKNOWLEDGMENT

This work was supported in part by the National Science Foundation and the U.S. Department of Energy. Y.J.P.T. acknowledges support from the National Science Foundation Materials Research Science and Engineering Center on Nanostructured Interfaces (MRSEC) and the Partnerships for Research and Education in Materials (PREM). H.N.P. acknowledges support from the National Science Foundation under Award No. EEC-0813570. The work at Argonne National Laboratory is based upon work supported as part of the Institute for Atom-efficient Chemical Transformations (IACT), an Energy Frontier Research Center funded by the U.S. Department of Energy, Office of Science, Office of Basic Energy Sciences.

■ REFERENCES

(1) Corma, A.; Iborra, S.; Velty, A. *Chem. Rev.* **2007**, *107*, 2411.
(2) Chheda, J. N.; Huber, G. W.; Dumesic, J. A. *Angew. Chem., Int. Ed.* **2007**, *46*, 7164.
(3) Serrano-Ruiz, J. C.; Dumesic, J. A. *ChemSusChem* **2009**, *2*, 581.
(4) West, R. M.; Braden, D. J.; Dumesic, J. A. *J. Catal.* **2009**, *262*, 134.
(5) Tanabe, K. *Catal. Today* **2003**, *78*, 65.
(6) Okuhara, T. *Chem. Rev.* **2002**, *102*, 3641.
(7) Carniti, P.; Gervasini, A.; Biella, S.; Auroux, A. *Catal. Today* **2006**, *118*, 373.
(8) Carniti, P.; Gervasini, A.; Biella, S.; Auroux, A. *Chem. Mater.* **2005**, *17*, 6128.
(9) Nowak, I.; Ziolek, M. *Chem. Rev.* **1999**, *99*, 3603.
(10) Florentino, A.; Cartraud, P.; Magnoux, P.; Guisnet, M. *Appl. Catal., A* **1992**, *89*, 143.
(11) Tanabe, K. *Mater. Chem. Phys.* **1987**, *17*, 217.
(12) Pham, H. N.; Pagan-Torres, Y. J.; Serrano-Ruiz, J. C.; Wang, D.; Dumesic, J. A.; Datye, A. K. *Appl. Catal., A* **2011**, *397*, 153.
(13) Lee, B.; Lu, D.; Kondo, J. N.; Domen, K. *J. Am. Chem. Soc.* **2002**, *124*, 11256.
(14) Antonelli, D. M.; Ying, J. Y. *Angew. Chem., Int. Ed.* **1996**, *35*, 426.
(15) Yang, P.; Zhao, D.; Margolese, D. I.; Chmelka, B. F.; Stucky, G. D. *Nature* **1998**, *396*, 152.
(16) Tanaka, M.; Shima, H.; Yokoi, T.; Tatsumi, T.; Kondo, J. N. *Catal. Lett.* **2011**, *141*, 283.
(17) Schüth, F. *Chem. Mater.* **2001**, *13*, 3184.
(18) Yuan, L.; Guliants, V. *J. Mater. Sci.* **2008**, *43*, 6278.
(19) Rao, Y.; Trudeau, M.; Antonelli, D. *J. Am. Chem. Soc.* **2006**, *128*, 13996.

(20) Nakajima, K.; Fukui, T.; Kato, H.; Kitano, M.; Kondo, J. N.; Hayashi, S.; Hara, M. *Chem. Mater.* **2010**, *22*, 3332.
(21) Krishnan, C. K.; Hayashi, T.; Ogura, M. *Adv. Mater.* **2008**, *20*, 2131.
(22) Segura, Y.; Cool, P.; Kustrowski, P.; Chmielarz, L.; Dziembaj, R.; Vansant, E. F. *J. Phys. Chem. B* **2005**, *109*, 12071.
(23) Hess, C.; Hoefelmeyer, J. D.; Tilley, T. D. *J. Phys. Chem. B* **2004**, *108*, 9703.
(24) Du, G.; Lim, S.; Pinault, M.; Wang, C.; Fang, F.; Pfefferle, L.; Haller, G. L. *J. Catal.* **2008**, *253*, 74.
(25) Herrera, J. E.; Kwak, J. H.; Hu, J. Z.; Wang, Y.; Peden, C. H. F.; Macht, J.; Iglesia, E. *J. Catal.* **2006**, *239*, 200.
(26) Law, H. Y.; Blanchard, J.; Carrier, X.; Thomas, C. *J. Phys. Chem. C* **2010**, *114*, 9731.
(27) Hakim, L. F.; McCormick, J. A.; Zhan, G. D.; Weimer, A. W.; Li, P.; George, S. M. *J. Am. Ceram. Soc.* **2006**, *89*, 3070.
(28) Zhang, J; Ma, Z.; Jiao, J.; Yin, H.; Yan, W.; Hagaman, E. W.; Yu, J.; Dai, S. *Langmuir* **2009**, *25*, 12541.
(29) Elam, J. W.; Routkevitch, D.; Mardilovich, P. P.; George, S. M. *Chem. Mater.* **2003**, *15*, 3507.
(30) Mahurin, S.; Bao, L.; Yan, W.; Liang, C.; Dai, S. *J. Non-Cryst. Solids* **2006**, *352*, 3280.
(31) Palkovits, R. *Angew. Chem., Int. Ed.* **2010**, *49*, 4336.
(32) Zhao, D.; Huo, Q.; Feng, J.; Chmelka, B. F.; Stucky, G. D. *J. Am. Chem. Soc.* **1998**, *120*, 6024.
(33) Elam, J. W.; Groner, M. D.; George, S. M. *Rev. Sci. Instrum.* **2002**, *73*, 2981.
(34) Libera, J. A.; Elam, J. W.; Pellin, M. J. *Thin Solid Films* **2008**, *516*, 6158.
(35) Gaertner, C. A.; Serrano-Ruiz, J. C.; Braden, D. J.; Dumesic, J. A. *J. Catal.* **2009**, *266*, 71.
(36) Kukli, K.; Ritala, M.; Leskela, M.; Lappalainen, R. *Chem. Vap. Deposition* **1998**, *4*, 29.
(37) Knapas, K.; Rahtu, A.; Ritala, M. *Langmuir* **2009**, *26*, 848.
(38) Haukka, S.; Kytökivi, A.; Lakomaa, E. L.; Lehtovirta, U.; Lindblad, M.; Lujala, V.; Suntola, T. *Stud. Surf. Sci. Catal.* **1995**, *91*, 957.
(39) Farmer, D. B.; Gordon, R. G. *Nano Lett.* **2006**, *6*, 699.
(40) Grubbs, R. K.; Nelson, C. E.; Steinmetz, N. J.; George, S. M. *Thin Solid Films* **2004**, *467*, 16.
(41) Hsu, I. J.; Hansgen, D. A.; McCandless, B. E.; Willis, B. G.; Chen, J. G. *J. Phys. Chem. C* **2011**, *115*, 3709.
(42) Alexandridis, P.; Olsson, U.; Lindman, B. *Langmuir* **1998**, *14*, 2627.
(43) Gallo, J. M. R.; Pastore, H. O.; Schuchardt, U. *J. Catal.* **2006**, *243*, 57.
(44) Sauer, J.; Marlow, F.; Schüth, F. *Phys. Chem. Chem. Phys.* **2001**, *3*, 5579.
(45) Gallo, J. M. R.; Bisio, C.; Gatti, G.; Marchese, L.; Pastore, H. O. *Langmuir* **2010**, *26*, 5791.
(46) Jehng, J. M.; Wachs, I. E. *Chem. Mater.* **1991**, *3*, 100.
(47) Wachs, I. E.; Roberts, C. A. *Chem. Soc. Rev.* **2010**, *39*, 5002.
(48) Burcham, L. J.; Datka, J.; Wachs, I. E. *J. Phys. Chem. B* **1999**, *103*, 6015.
(49) Lowell, S.; Shields, J. E.; Thomas, M. A.; Thommes, M. *Characterization of porous solids and powders: surface area, pore size and density*, 1st ed.; Springer: Dordrecht, The Netherlands, 2006.
(50) Ravikovitch, P. I.; Haller, G. L.; Neimark, A. V. *Adv. Colloid Interface Sci.* **1998**, *76*, 203.
(51) Thommes, M.; Kohn, R.; Froba, M. *Appl. Surf. Sci.* **2002**, *196*, 239.
(52) Kruk, M.; Antochshuk, V.; Jaroniec, M.; Sayari, A. *J. Phys. Chem. B* **1999**, *103*, 10670.
(53) Abdel-Rehim, M. A.; dos Santos, A. C. B.; Camorim, V. L. L.; da Costa Faro, J. A. *Appl. Catal., A* **2006**, *305*, 211.
(54) Asakura, K.; Iwasawa, Y. *Chem. Lett.* **1986**, 859.
(55) Shirai, M.; Asakura, K.; Iwasawa, Y. *J. Phys. Chem.* **1991**, *95*, 9999.
(56) Tang, Q.; Hu, S.; Chen, Y.; Guo, Z.; Hu, Y.; Chen, Y.; Yang, Y. *Microporous Mesoporous Mater.* **2010**, *132*, 501.
(57) Galarneau, A.; Nader, M.; Guenneau, F.; Di Renzo, F.; Gedeon, A. *J. Phys. Chem. C* **2007**, *111*, 8268.
(58) Zhang, F.; Yan, Y.; Yan, H.; Meng, Y.; Yu, C.; Tu, B.; Zhao, D. *J. Phys. Chem. B* **2005**, *109*, 8723.
(59) Weissman, J. G.; Ko, E. I.; Wynblatt, P. *J. Catal.* **1987**, *108*, 383.
(60) Ouqour, A.; Coudurier, G.; Vedrine, J. C. *J. Chem. Soc., Faraday Trans.* **1993**, *89*, 3151.
(61) Luy, J. C.; Parera, J. M. *Appl. Catal.* **1986**, *26*, 295.
(62) Gervasini, A.; Bellussi, G.; Fenyvesi, J.; Auroux, A. *J. Phys. Chem.* **1995**, *99*, 5117.
(63) Ziolek, M. *Catal. Today* **2003**, *78*, 47.
(64) Guo, C.; Qian, Z. *Catal. Today* **1993**, *16*, 379.
(65) Serrano-Ruiz, J. C.; Wang, D.; Dumesic, J. A. *Green Chem.* **2010**, *12*, 574.
(66) Bozell, J. J. *Science* **2010**, *329*, 522.
(67) Lange, J. P.; Price, R.; Ayoub, P. M.; Louis, J.; Petrus, L.; Clarke, L.; Gosselink, H. *Angew. Chem., Int. Ed.* **2010**, *49*, 4479.
(68) Bond, J. Q.; Martin Alonso, D.; West, R. M.; Dumesic, J. A. *Langmuir* **2010**, *26*, 16291.